Journal of Materials Chemistry C

PAPER

View Article Online
View Journal | View Issue

Cite this: J. Mater. Chem. C, 2017, 5, 10399

Temperature regulation growth of Au nanocrystals: from concave trisoctahedron to dendritic structures and their ultrasensitive SERS-based detection of lindane†

Xia Zhou,[abc] Qian Zhao,[ab] Guangqiang Liu,*[a] Hongwen Zhang,[a] Yue Li[a] and Weiping Cai*[ab]

Received 21st August 2017,
Accepted 13th September 2017

DOI: 10.1039/c7tc03808a

rsc.li/materials-c

A facile temperature regulation strategy is developed for fabrication of Au concave nanocrystals with specific shapes *via* seed-assisted growth at 25 °C or lower. It has been found that the reaction temperature, even with minor changes, can significantly influence the shape of the nanocrystals, which evolves from the concave trisoctahedral to calyptriform, coral and dendritic structures with the decrease of temperature from 25 °C to 5 °C. The size and optical absorbance spectra of the nanocrystals can be determined just by the addition amount of Au seeds. The formation of the Au concave nanocrystals is attributed to the preferential growth of the nuclei in ⟨110⟩ and ⟨111⟩ directions, along which the growth rates are of different temperature dependences. Importantly, the concave trisoctahedral and calyptriform Au nanocrystal-built films have exhibited strong surface enhanced Raman scattering (SERS) activity towards the lindane molecules, with the enhancement factor higher than 10^7, due to their high density of sharp corners/edges or the tip effect. The Raman peak intensity *versus* lindane concentration is subject to a linear double logarithmic relation from 30 ppb to 300 ppm, which is attributed to the Freundlich adsorption of lindane molecules on the Au nanocrystals. This work provides not only a simple route for the fabrication of the Au nanocrystals with various specific structures but also efficient SERS substrates for trace detection of organochlorine pesticide residues.

1. Introduction

Nanocrystals with different shapes such as spheres, cubes, polyhedrons, bipyramids, plates, rods and wires have extensively been reported.[1–4] All of these nanocrystals are enclosed by convex surfaces and low-index facets. Compared with these convex systems, the concave and dendritic nanocrystals consist of high-index facets and a high density of sharp corners/edges, and possess distinctive optical and catalytic properties.[5–8] Such nanocrystals, especially for noble metals, have received increasing interest in recent years due to their potential applications in surface enhanced Raman scattering (SERS) substrates,[9,10] plasmonics,[11,12] catalysis,[13,14] *etc.* Particularly, for the concave and dendritic Au or Ag nanocrystals, they show strong SERS activity due to the presence of large numbers of tips and edges which can serve as hot spots induced by the large electric-field enhancement.[15,16]

There have been some reports on noble metal concave[5,6,16–20] and dendritic[21–24] nanocrystals, which were fabricated mainly using a seed-mediated growth method and the solution-phase synthesis route. For instance, Mirkin *et al.* synthesized the concave Au nanocubes in the growth solution with cetyltrimethylammonium chloride (CTAC) and L-ascorbic acid (AA) *via* seed-mediated growth at room temperature.[6] Xia *et al.* fabricated the Ag concave octahedrons and cubes in the growth solution with reductant AA and Ag nanocubic seeds at room temperature.[16] Wang *et al.* obtained Au concave nanocubes, trisoctahedral and star-like Au nanocrystals in the seed-containing solution at room temperature.[20] Lyu *et al.* developed a facile solution synthesis method for the Ag concave nanocrystals with various shapes from cubic to octahedral and hexapod structures.[21] The seed-mediated growth route at room temperature requires precise control of the adding amount of the precursor containing $HAuCl_4$ or $AgNO_3$ solution and reducer to adjust the reaction rate, while the solution-phase synthesis method needs the

[a] Key Lab of Materials Physics, Anhui Key Lab of Nanomaterials and Nanotechnology, Institute of Solid State Physics, Chinese Academy of Sciences, Hefei 230031, P. R. China. E-mail: liugq@issp.ac.cn, wpcai@issp.ac.cn
[b] University of Science and Technology of China, Hefei 230026, P. R. China
[c] School of Chemistry and Chemical Engineering, Suzhou University, Suzhou, Anhui 234000, P. R. China

† Electronic supplementary information (ESI) available: The XRD patterns, optical absorbance spectra, SEM images of the products obtained at different reaction temperatures, the Raman spectra of the lindane molecules on Au nanocrystal films. See DOI: 10.1039/c7tc03808a

metal carbonyl compounds as additives or for regulation of the proportion of various reactants. On the whole, these two kinds of methods are not easy to control and operate. The fabrication of concave or dendritic nanocrystals with controllable structures in a simple and facile way is still awaited.

Herein, we develop a facile and simple route to the Au concave nanocrystals with various specific shapes based on the temperature regulated seed-assisted strategy, or *via* dropping the Au seed solution into the growth solution containing the surfactant and reducer at 25 °C or lower. Our experiments have shown that the reaction temperature, even with minor changes, can significantly influence the morphology of nanocrystals, which evolves from the concave trisoctahedral to calyptriform, coral and dendritic structures with the decrease of the temperature from 25 °C down to 5 °C, while the addition amount of Au seeds can only influence the size and optical absorbance spectra of the nanocrystals, and shows increase and red-shift with decrease of the addition amount, respectively. Importantly, the concave trisoctahedral and calyptriform Au nanocrystal-built films have exhibited a strong SERS activity towards lindane molecules, with the enhancement factor higher than 10^7. The Raman peak intensity *versus* the lindane concentration is subject to a linear double logarithmic relation in the range of 30 ppb to 300 ppm. This study provides not only a simple route for the fabrication of the Au nanocrystals with specific structures *via* temperature regulation but also to the efficient SERS substrates for the trace detection of organochlorine pesticide residues.

2. Experimental

2.1 Materials

Gold(III) chloride ($HAuCl_4 \cdot 4H_2O$), and 4-aminothiophenol (C_6H_7NS, 4-ATP, 97%) were obtained from Alfa Aesar Chemical Reagent Tianjin Co., Ltd. Sodium borohydride ($NaBH_4$, 99%), hexadecyltrimethylammonium chloride (CTAC, 96%), L-ascorbic acid (AA, 99.5 + %) and ethanol were purchased from Sinopharm Chemical Reagent Beijing Co., Ltd. Lindane was purchased from J&K Chemical Scientific Shanghai Co., Ltd. All reagents were used as received without further purification. Ultrapure water (18.2 MΩ in resistivity, Barnstead Easy Pure II 7138) was used for all experiments.

2.2 Preparation of Au nanocrystals

In this work, the Au nanocrystals were fabricated *via* a modified seed-assisted growth with temperature regulation. Firstly, the colloidal solution of the Au seeds of about 3 nm in size was prepared by addition of appropriate amounts of $NaBH_4$ in the $HAuCl_4$ aqueous solution containing CTAC, as previously reported.[20] Typically, 0.30 mL ice-cold, freshly prepared $NaBH_4$ aqueous solution (10 mM) was injected into 10 mL aqueous solution with CTAC (0.10 M) and $HAuCl_4$ (0.25 mM) at 25 °C. The Au seeds were formed in the solution after being undisturbed for 2 h. Then, the seed solution was diluted to 1000-fold by using CTAC aqueous solution for subsequent use.

Au nanocrystals were then prepared by seed-assisted growth at different temperatures. Briefly, 0.05 mL diluted Au seed solution was added to 10 mL growth solution containing $HAuCl_4$ (0.50 mM), AA (10 mM) and CTAC (0.10 M) in a flask, and the flask with the mixed solution was left undisturbed for 4 h in the water bath at a given temperature (from 5 °C to 100 °C). After reaction, the products or Au nanocrystals were washed with deionized water twice through centrifugation and finally collected in 1.0 mL water to form the colloidal solution.

2.3 Characterization

The morphology of the products was observed on a field emission scanning electron microscope (FESEM, FEI Sirion 200) equipped with an Oxford IE250X-Max50 energy dispersion spectroscope (EDS). X-ray diffraction (XRD) patterns were recorded on an X'Pert Philips diffractometer using Cu Kα radiation (0.15406 nm). Microstructural examination was performed on a transmission electron microscope (TEM, JOEL JEM-2100) operated at 120 kV. The optical absorbance spectra were measured with a Shimadzu UV-3100 spectrometer.

2.4 The SERS measurements

Au nanocrystal-built films were firstly prepared by alternatively dropping the as-prepared colloidal solution on the silicon wafer and drying to form the thin film substrates. After that, the thin film substrates were immersed into 5 mL lindane ethanol solution with a certain concentration for 8 h. The soaked substrates were then taken out, and rinsed with deionized water and ethanol to remove any unbound molecules. Finally, Raman spectral measurements were conducted at room temperature on a confocal Raman spectrometer (Renishaw Invia Raman Microscope) excited with a laser of 785 nm in wavelength and 2 mW in power. The laser spot size on the sample was 1 μm in diameter and the integral time was 5 s.

3. Results and discussion

After dropping the 0.05 mL diluted Au seed solution into the growth solution at 25 °C and reaction for 4 h, the colloidal solution was obtained, as shown in the inset of Fig. 1a. Fig. 1a shows the corresponding optical absorbance spectrum. There exists a strong peak around 600 nm, which corresponds to the

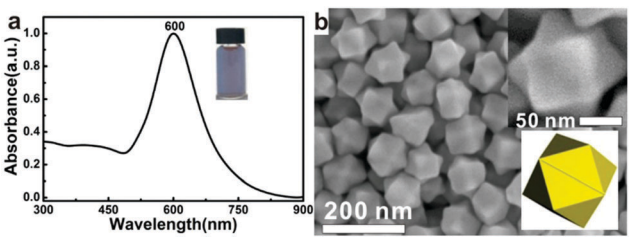

Fig. 1 (a) The optical absorbance spectrum of the as-prepared colloidal solution obtained by adding 0.05 mL Au seed solution into the growth solution at 25 °C. The inset is the photo of the colloidal solution. (b) The SEM image corresponding to the products in (a). The insets are the SEM image and geometric model of an individual Au concave trisoctahedron.

dipolar localized surface plasmon resonance (SPR) of Au nanoparticles[25] and indicates the formation of Au nanocrystals in the solution. Further, the XRD measurements have also confirmed that the products in the solution are Au crystals, as shown in Fig. S1 (ESI†).

The corresponding morphological observation shows that the products in the as-prepared colloidal solution consist of nearly equiaxed polyhedral particles of about 100 nm in size, as typically illustrated in Fig. 1b. These polyhedral particles are actually the concave trisoctahedrons comprising eight trigonal pyramids and generated from an octahedron by ''pulling out'' the centers of the eight triangular {111} facets,[26] as shown in the inset of Fig. 1b. All the 24 facets of a trisoctahedron belong to the crystal planes of the family of the ⟨110⟩ zone axis.[16] Almost all particles in the products are concave trisoctahedrons, although some particles did not appear to be trisoctahedral due to different orientations. These are in agreement with those reported previously.[25]

It has been found that the addition amount of Au seeds could significantly change the final size of the Au nanocrystals, and thus further influence the optical absorption peak position of the Au colloidal solution. The SPR red-shifts from 575 nm to 780 nm with decrease of the Au seed solution amount from 0.1 mL to 0.01 mL, as shown in Fig. S2 (ESI†). Correspondingly, decreasing the seed amount induces the significant increase of the particle size from 80 nm to 135 nm, but with nearly unchanged particle shape (still concave trisoctahedron), as illustrated in Fig. S3 (ESI†). So, the dipolar local SPR of the Au concave trisoctahedral nanoparticles red-shifts with the increasing particle size.

3.1 Reaction temperature-dependent morphology

When the reaction temperature was >25 °C up to 100 °C, it has been found that the products are still Au concave trisoctahedral nanoparticles, as typically shown in Fig. S4 (ESI†). The size of nanocrystals is nearly unchanged although the corners/edges tend to be truncated or smooth with the increase of the reaction temperature.

However, when the temperature is below 25 °C, the shape of the nanocrystals is very sensitive to the reaction temperature, and a small temperature change would significantly affect the morphology. When the temperature was decreased from 25 °C to 20 °C, the Au nanoparticles were significantly changed in morphology from concave trisoctahedron to the calyptriform but with a nearly unchanged size (about 100 nm), as shown in Fig. 2a. If the temperature was further decreased to 10 °C and 5 °C, coral and even dendritic nanoparticles were formed, respectively, as illustrated in Fig. 2b and c. The Au nanocrystals obtained under different reaction temperatures are very uniform in size and morphology. Furthermore, the TEM examination was conducted. Typically, Fig. 2 shows the single concave structured nanocrystals obtained under different temperatures. In addition, the XRD measurements have also confirmed that the products obtained under different reaction temperatures are Au crystals, as shown in Fig. S1 (ESI†). Here, we did not do the experiment below 5 °C since the CTAC in the solution would crystallize and precipitate at such a low temperature leading to the concentration change of the growth solution.

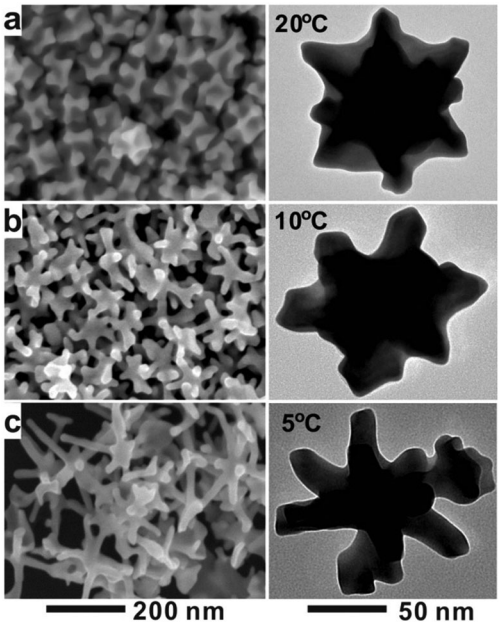

Fig. 2 SEM (left frames) and TEM (right frames) images of the products obtained under different reaction temperatures with addition of a 0.05 mL seed solution. (a) 20 °C, (b) 10 °C, (c) 5 °C.

Similarly, the increase of the addition amount of the Au seed solution would lead to the decrease of Au nanocrystals in size, but the morphology was nearly unchanged for each reaction temperature (Fig. S5–S7, ESI†). The SPR of the corresponding Au nanocrystals red-shifts with decreasing the addition amount of the Au seed solution or the increasing particle size, as clearly demonstrated in Fig. 3. Typically, for the Au nanocrystals obtained at 20 °C, when the addition amount decreased from 0.1 mL to 0.01 mL, the SPR peak red-shifted from 581 nm to 776 nm, and the corresponding particle size increased from about 90 nm to 190 nm. Therefore, the size of Au nanocrystals can easily be tuned without morphological change just by changing the seed' amount. In addition, as the particle size increased, the dipolar SPR became increasingly broadened, and a narrower quadrupolar SPR emerged at a shorter wavelength than the dipolar one and became increasingly pronounced as the size of the nanocrystals increased due to the phase retardation effects.[27]

3.2 Temperature-controlled preferential growth

Now let us start a brief discussion on the formation of Au nanocrystals with the temperature-dependent shape.

In the seed solution, the Au^{3+} ions would be reduced to Au^0 by $NaBH_4$, according to the reaction:

$$AuCl_4^- + 3e^- \rightarrow Au^0 + 4Cl^- \quad (1)$$

However, in the growth solution, the reduction capacity of AA is weaker than that of $NaBH_4$.[28–30] So the Au^{3+} ions would be only reduced to Au^+ according to the reaction:

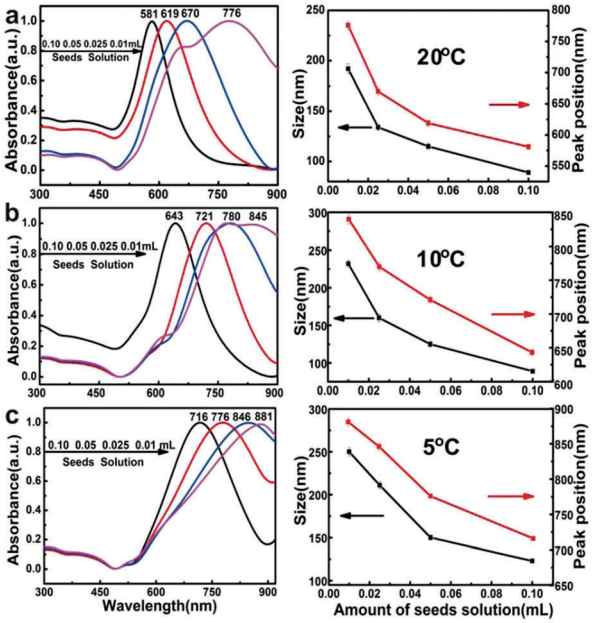

Fig. 3 Influences of the addition amount of Au seeds solution on the optical absorbance spectra of the colloidal solutions obtained under different reaction temperatures (left column), particle size and SPR position (right column). (a) 20 °C, (b) 10 °C, (c) 5 °C.

$$AuCl_4^- + 2e^- \rightarrow AuCl_2^- + 2Cl^- \quad (2)$$

When the Au seed solution was added into the growth solution, the Au^+ ions would be reduced to Au^0 due to the abundant electrons provided by the excess reducing agent $NaBH_4$ in the seed solution,[28–30] or the reaction

$$AuCl_2^- + e^- \rightarrow Au^0 + 2Cl^- \quad (3)$$

would take place. The partial Au^0 would form Au^0-CTAC complexes with the surfactants, according to the previous report.[28] The complexes and the reduced free Au^0 atoms co-exist in the growth solution. The complexes would preferentially be adsorbed on the {110} planes of the seeds due to the presence of the surfactant CTAC, while the free Au^0 atoms are preferentially attached or deposited on the {111} planes.[30] So the seeds grow along the ⟨110⟩ and ⟨111⟩ directions. Obviously, the growth rate is temperature-dependent, and the temperature-dependent growth rates should be different for both directions, which induce the Au nanocrystals with reaction temperature-dependent morphology, as shown in Fig. 1 and 2.

At 25 °C, the growth rates in both directions are close, leading to the formation of the concave trisoctahedron as shown in Fig. 1b. When the temperature was higher than 25 °C, the growth rates in both directions were increasing but getting closer. So the Au nanocrystal shapes tend to be truncated and smooth with the increase of the reaction temperature.

However, when the reaction temperature was lower than 25 °C, the growth rates in both directions decreased. But the growth rate along ⟨110⟩ was, relatively, increasingly faster than that along ⟨111⟩ with decreasing the temperature due to the preferential adsorption of the surfactant CTAC, resulting in the formation of calyptriform, coral and even dendritic structures. For further confirmation, Fig. 4a shows the TEM image of the dendritic structure obtained at 5 °C, Fig. 4b gives the HRTEM image of the trunk's top area marked in Fig. 4a. It has been shown that the dendritic growth is along the [110] direction.

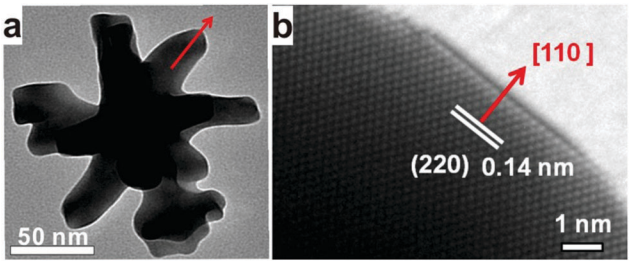

Fig. 4 (a) TEM image of a single dendritic Au nanocrystal obtained at 5 °C. (b) HRTEM image of the trunk's top area marked in (a).

As for the influence of the seed amount, since the added Au seeds correspond to the nuclei of Au nanocrystals, decrease in the addition amount of seed solution would reduce the number of the Au nanoparticles in the growth solution, and hence induce increase of the final nanocrystals in size but with an insignificant change in morphology under the given temperatures (Fig. S5–S7, ESI†). Also the increase in size would lead to red-shift of the SPR (Fig. 3).[20]

3.3 Concave Au nanocrystal-based SERS substrates for the detection of lindane

The Au concave and dendritic nanocrystals can generate intense local-field enhancements at their edges, sharp corners and gaps under external field excitation, and exhibit a strong SERS effect.[10,13,23,31] Here, we use lindane (γ-666), an organochlorine pesticide, as the target molecule to study the SERS performances of the concave and dendritic nanocrystals mentioned above.

Lindane or its isomers are a kind of organochlorine pesticide and belong to the group of highly toxic substances.[32,33] Currently, they are usually analysed and detected using gas chromatography equipped with electron capture detection (GC/ECD) and the gas chromatography-mass spectrometry (GC-MS) coupling technique.[34,35] Such conventional analysis methods are complex and time-consuming. The SERS-based method could be a promising route to the quick and ultrasensitive detection of toxic molecules.[36–38] However, the reports on the SERS-based detection of lindane are very limited.

3.3.1 SERS activity of the concave nanocrystals. The different Au nanocrystal-built films with a certain thickness were first prepared by alternatively dropping the as-prepared colloidal solutions on silicon wafers and drying, as typically shown in Fig. S8 (ESI†). It has been shown that such prepared nanocrystal-built films are uniform in structure and hence have good reproducibility in Raman spectral measurements. The maximal standard deviation values for all samples are below 15%, as shown in Fig. S9 and S10 (ESI†). Also, the film's thickness would affect the SERS performances when the film is not thick enough or the film thickness is smaller than the

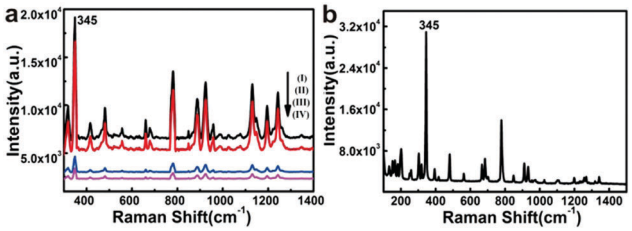

Fig. 5 The Raman spectra of lindane molecules on the different substrates. (a). The SERS spectra for the films of the Au nanocrystals obtained under the reaction temperatures (I) 25 °C, (II) 20 °C, (III) 10 °C and (IV) 5 °C, after soaking in the lindane ethanol solution of 10^{-5} M for 8 h. (b) The Raman spectrum of the solid lindane.

penetration depth of the laser beam into the thin film. In this study, it has been found that when the film thickness reaches 500 nm or larger, the Raman signals are independent of the thickness, as typically demonstrated in Fig. S11 (ESI†). Furthermore, the influence of the excitation wavelength on the SERS activity was examined. It has been shown that the optimum excitation wavelength is 785 nm for the Au nanocrystal-built films, as illustrated in Fig. S12 (ESI†). On the basis of the above, here the Au nanocrystal-built films of 500 nm in thickness were used as SERS substrates, and an excitation of 785 nm was employed. Fig. 5a shows the Raman spectra of the different Au nanocrystal-built films after soaking in lindane ethanol solution with 10^{-5} M for 8 h. Except for the peak intensity, these soaked films show the same Raman spectral pattern, which is in good agreement with that of the solid lindane, as shown in Fig. 5b. The main peak at 345 cm^{-1} is attributed to the stretching vibrations of C–Cl in lindane.[38–40]

From Fig. 5, the intensities of the main peak for these soaked films are comparable to that of the pure solid lindane, indicating the significantly enhanced effect. Further, the intensities of Raman peaks for the lindane molecules on the trisoctahedral nanocrystals are the strongest, and those on the calyptriform nanocrystals are slightly lower, while the coral and the dendritic structured nanocrystals show much lower Raman intensities. For quantification, the enhancement factor (EF) was estimated according to[41,42]

$$\mathrm{EF} = \frac{I_{\mathrm{SERS}}/N_{\mathrm{SERS}}}{I_{\mathrm{RS}}/N_{\mathrm{RS}}} \quad (4)$$

where I_{SERS} and I_{RS} are the intensities of the selected Raman peaks (or 345 cm^{-1} here) of lindane molecules on the substrates with and without the enhanced effect [or the Au nanocrystals and Si substrate in this study], respectively. N_{SERS} and N_{RS} are the corresponding numbers of the lindane molecules within the laser spot areas (ϕ 1 μm). In order to obtain the value of N_{SERS} and N_{RS}, we re-measured the Raman spectra of the lindane molecules by dropping the 20 μL of 10^{-5} M and 50 μL of 0.1 M lindane solutions on the Au nanocrystal films (with circle area about ϕ 3 mm in diameter) and a Si substrate of 3 mm × 3 mm in area respectively. The corresponding Raman spectra are given in Fig. S13 (ESI†). Here, we assume that all the lindane molecules were adsorbed and distributed uniformly in these areas after drying. The values of N_{SERS} and N_{RS} could thus be estimated to be about 1.3×10^7 and 3.2×10^{11}, respectively. According to eqn (4), the EF values for the different Au nanocrystals could be calculated for the vibration at 345 cm^{-1}, as listed in Table 1. The four concave Au nanocrystals presented in this study show strong SERS activity to the lindane molecules, and their EF values are higher than 10^6, especially for the concave trisoctahedral and calyptriform nanocrystals, which show EF values higher than 10^7.

Table 1 The measured EF values of the different Au nanocrystals for lindane molecules at 345 cm^{-1}

Substrates	Trisoctahedral	Calyptriform	Coral	Dendritic
EF	1.9×10^7	1.6×10^7	1.8×10^6	1.1×10^6

3.3.2 Concentration dependent Raman spectra. Comparatively, the trisoctahedral nanocrystals show the highest SERS activity to lindane molecules among the four nanocrystals, as presented in Table 1. The trisoctahedral nanocrystal-built film was thus used as a SERS substrate to measure the concentration dependent Raman spectra of lindane molecules. Fig. 6a shows the Raman spectra of the film after immersion in the lindane solutions with different concentrations.

All peaks increase in intensity with the rising of the lindane concentration in the soaking solutions. The lower detection limit was 10^{-7} M (or 30 ppb). So, such a trisoctahedral nanocrystal-built film could be used as a substrate for SERS-based detection of trace lindane molecules in solutions. Further, concentration dependent Raman peak intensity I could quantitatively be described by the double logarithmic linear relation with lindane concentration C in the soaking solution, or

$$\log(I) = A + B\log(C) \quad (5)$$

where A and B are the constants independent of the concentration, and C is in molar concentration. Fig. 6b shows the representative result corresponding to the main peaks at 345 cm^{-1}, exhibiting a good double logarithmic linear relation in the range of 10^{-7} M to 10^{-3} M (or 30 ppb to 300 ppm). Furthermore, the values of parameters A and B are 3.51 and 0.28, respectively, by fitting. We can thus re-write eqn (5) as a power function, or

$$I = 3236 \times C^{0.28} \quad (6)$$

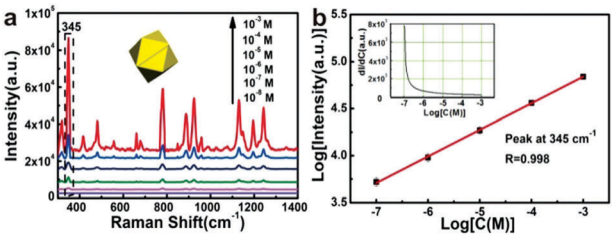

Fig. 6 (a) The Raman spectra of the trisoctahedral nanocrystal-built film after immersion in lindane ethanol solutions with different concentrations from 10^{-3} M to 10^{-8} M. (b) Double logarithmic plot of the peak intensity at 345 cm^{-1} *versus* lindane concentration (C) [data from (a)]. The straight-line is the linear fitting result and R is the correlation coefficient. The inset in (b): the Raman sensitivity as a function of the lindane concentration.

Also, we can get the concentration dependence of the sensitivity, or

$$dI/dC = 906 \times C^{-0.72} \quad (7)$$

The sensitivity of the Raman signal as a function of the lindane concentration is illustrated in the inset of Fig. 6b. Obviously, the lower concentration corresponds to the higher sensitivity. Detection based on the SERS effect is thus suitable for trace amounts of lindane.

3.3.3 Tip-induced strong SERS effect and Freundlich adsorption model of lindane molecules. As mentioned above, the enhancement factors of the trisoctahedral and calyptriform Au nanocrystals are much higher than those of the coral and dendritic ones. This is attributed to their special structures. There exists a much higher number density at the tips or the sharp corners/edges in the trisoctahedral or calyptriform nanocrystal-built film than that in the coral and dendritic ones, as clearly demonstrated in Fig. S8 (ESI†). Due to the tip-effect, the sharp corners/edges would induce the strong electromagnetic field enhancement under external field excitation.[43] In addition, the nano-gaps among the nanocrystals in the films are also the "hot spots" with significant local-field enhancement effect due to surface plasmonic coupling effects.[44–47] It is the high number density of the sharp corners/edges that provides the trisoctahedral or calyptriform Au nanocrystals with the strongest SERS activity.

The high sensitivity at low concentrations of lindane could be attributed to the concentration-dependent adsorption. After the Au nanocrystal film was immersed in the lindane solution for sufficient time, equilibrium adsorption of the lindane molecules on the Au nanocrystals would be reached. The intensity or integral area of a Raman peak should be proportional to the number of the molecules adsorbed on the nanocrystal film within the area of a laser spot, or show a linear relation with the equilibrium adsorption amount q_e:

$$I = K_1 \cdot q_e \quad (8)$$

where K_1 is the constant. Obviously, the higher lindane concentration in the solution would lead to the more lindane molecules adsorbed on the film, which thus induces stronger Raman signals, exhibiting increase of the Raman peak intensity with rising lindane concentration in the soaking solutions, as shown in Fig. 6a.

Further, in this study, the concentration dependence of Raman peak intensity is subject to a power function [see eqn (6)]. It is known that the equilibrium adsorption of molecules on a heterogeneous surface could be described by the Freundlich model,[48–50] or

$$q_e = K_F \cdot C^{1/n} \quad (9)$$

where the parameters K_F and n are the parameters reflecting the adsorption capacity and adsorption intensity, respectively. By combining eqn (8) and (9), we have the relationship between the Raman intensity and the lindane concentration in the soaking solutions, or

$$I = K \cdot C^{1/n} \quad (10)$$

where $K = K_1 \cdot K_F$. Obviously, eqn (10) is in agreement with eqn (6). Such an agreement has also confirmed that the adsorption of the lindane molecules on the Au nanocrystals follows the Freundlich model. Comparing eqn (6) with (10), we can thus obtain the parameter value of lindane adsorption, $n = 3.57$. This also provides a simple and convenient method to determine the adsorption parameters, which are usually obtained by the time consuming measurement of the adsorption isotherms.

4. Conclusions

In summary, we have developed a simple temperature regulated method to fabricate Au concave nanocrystals with various specific shapes. The shape of the nanocrystals evolves from concave trisoctahedral to calyptriform, coral, dendritic structures with decreasing the temperature from 25 °C down to 5 °C, while the size of the nanocrystals and the optical absorbance spectra exhibit an increase and a red-shift with reduction in the amount of seeds, respectively. The formation of the Au concave nanocrystals is attributed to the preferential growth in the ⟨110⟩ and ⟨111⟩ directions, along which the growth rates are of different temperature dependences, leading to the temperature-dependent morphological evolution of the Au nanocrystals. Importantly, because of the high number density of sharp corners/edges, the concave trisoctahedral and calyptriform Au nanocrystal-built films have exhibited strong SERS activity with the enhancement factor higher than 10^7 towards lindane molecules. The Raman peak intensity *versus* the lindane concentration is subject to a linear double logarithmic relation in the range of 30 ppb to 300 ppm, which is attributed to the Freundlich adsorption of lindane molecules on the Au nanocrystals. This study has provided a facile approach for the fabrication of the Au nanocrystals with various specific structures *via* temperature regulation, and presented efficient SERS substrates for trace detection of organochlorine pesticide residues.

Conflicts of interest

There are no conflicts to declare.

Acknowledgements

This work is financially supported by the National Key Research and Development Program of China (Grant No. 2017YFA0207101), the Natural Science Foundation of China (Grant No. 51531006, 11574313, 11374300 and 51571188), and the CAS/SAF International Partnership Program for Creative Research Teams.

Notes and references

1 N. R. Jana, L. Gearheart and C. J. Murphy, *Chem. Commun.*, 2001, 617.
2 Y. G. Zhang, F. Lu, K. G. Yager, D. van der Lelie and O. Gang, *Nat. Nanotechnol.*, 2013, **8**, 86.
3 Y. G. Sun and Y. N. Xia, *Science*, 2002, **298**, 2176.
4 C. C. Li, K. L. Shuford, Q. H. Park, W. P. Cai, Y. Li, E. J. Lee and S. O. Cho, *Angew. Chem., Int. Ed.*, 2007, **46**, 3264.

5 X. Q. Huang, S. H. Tang, H. H. Zhang, Z. Y. Zhou and N. F. Zheng, *J. Am. Chem. Soc.*, 2009, **131**, 13916.
6 J. A. Zhang, M. R. Langille, M. L. Personick, K. Zhang, S. Y. Li and C. A. Mirkin, *J. Am. Chem. Soc.*, 2010, **132**, 14012.
7 Y. L. Qin, X. B. Zhang, J. Wang and L. M. Wang, *J. Mater. Chem.*, 2012, **22**, 14861.
8 J. P. Lai, W. X. Niu, S. P. Li, F. X. Wu, R. Luque and G. B. Xu, *J. Mater. Chem. A*, 2016, **4**, 807.
9 Q. F. Zhang, Y. D. Zhou, E. Villarreal, Y. Lin, S. L. Zou and H. Wang, *Nano Lett.*, 2015, **15**, 4161.
10 J. W. Hong, S. U. Lee, Y. W. Lee and S. W. Han, *J. Am. Chem. Soc.*, 2012, **134**, 4565.
11 M. Rycenga, C. M. Cobley, J. Zeng, W. Y. Li, C. H. Moran, Q. Zhang, D. Qin and Y. N. Xia, *Chem. Rev.*, 2011, **111**, 3669.
12 A. J. Haes, C. L. Haynes, A. D. McFarland, G. C. Schatz, R. R. Van Duyne and S. L. Zou, *MRS Bull.*, 2005, **30**, 368.
13 H. Zhang, M. S. Jin and Y. N. Xia, *Angew. Chem., Int. Ed.*, 2012, **51**, 7656.
14 S. H. Joo, J. Y. Park, C. K. Tsung, Y. Yamada, P. D. Yang and G. A. Somorjai, *Nat. Mater.*, 2009, **8**, 126.
15 M. Rycenga, M. R. Langille, M. L. Personick, T. Ozel and C. A. Mirkin, *Nano Lett.*, 2012, **12**, 6218.
16 X. H. Xia, J. Zeng, B. McDearmon, Y. Q. Zheng, Q. G. Li and Y. N. Xia, *Angew. Chem., Int. Ed.*, 2011, **50**, 12542.
17 H. Zhang, W. Y. Li, M. S. Jin, J. E. Zeng, T. K. Yu, D. R. Yang and Y. N. Xia, *Nano Lett.*, 2011, **11**, 898.
18 C. L. Lu, K. S. Prasad, H. L. Wu, J. A. A. Ho and M. H. Huang, *J. Am. Chem. Soc.*, 2010, **132**, 14546.
19 Y. Liu, S. L. Liu, Z. W. Che, S. C. Zhao, X. X. Sheng, M. Han and J. C. Bao, *J. Mater. Chem. A*, 2016, **4**, 16690.
20 Q. Zhang, N. Large and H. Wang, *ACS Appl. Mater. Interfaces*, 2014, **6**, 17255.
21 L. M. Lyu, W. C. Wang and M. H. Huang, *Chem. – Eur. J.*, 2010, **16**, 14167.
22 Y. J. Kang, J. B. Pyo, X. C. Ye, R. E. Diaz, T. R. Gordon, E. A. Stach and C. B. Murray, *ACS Nano*, 2013, **7**, 645.
23 L. F. Zhang, S. L. Zhong and A. W. Xu, *Angew. Chem., Int. Ed.*, 2013, **52**, 645.
24 C. A. Garcia-Negrete, T. C. Rojas, B. R. Knappett, D. A. Jefferson, A. E. H. Wheatley and A. Fernandez, *Nanoscale*, 2014, **6**, 11090.
25 Y. Y. Ma, Q. Kuang, Z. Y. Jiang, Z. X. Xie, R. B. Huang and L. S. Zheng, *Angew. Chem., Int. Ed.*, 2008, **47**, 8901.
26 A. A. Proussevitch and D. L. Sahagian, *Comput. Geosci.*, 2001, **27**, 441.
27 H. Wang and N. J. Halas, *Adv. Mater.*, 2008, **20**, 820.
28 Z. L. Wang, R. P. Gao, B. Nikoobakht and M. A. El-Sayed, *J. Phys. Chem. B*, 2000, **104**, 5417.
29 J. Perez-Juste, L. M. Liz-Marzan, S. Carnie, D. Y. C. Chan and P. Mulvaney, *Adv. Funct. Mater.*, 2004, **14**, 571.
30 C. J. Murphy, T. K. San, A. M. Gole, C. J. Orendorff, J. X. Gao, L. Gou, S. E. Hunyadi and T. Li, *J. Phys. Chem. B*, 2005, **109**, 13857.
31 J. Zhang, S. A. Winget, Y. Wu, D. Su, X. Sun, Z. X. Xie and D. Qin, *ACS Nano*, 2016, **10**, 2607.
32 I. Lopez-Tocon, J. C. Otero, J. F. Arenas, J. V. Garcia-Ramos and S. Sanchez-Cortes, *Anal. Chem.*, 2011, **83**, 2518.
33 F. Peluso, S. Dubny, N. Othax and J. G. Castelain, *Hum. Ecol. Risk Assess.*, 2014, **20**, 1177.
34 X. Q. Xu, H. G. Yang, Q. L. Li, B. J. Yang, X. R. Wang and F. S. C. Lee, *Chemosphere*, 2007, **68**, 126.
35 M. Ali, A. A. Kazmi and N. Ahmed, *Chemosphere*, 2014, **102**, 68.
36 I. Izquierdo-Lorenzo, J. Kubackova, D. Manchon, A. Mosset, E. Cottancin and S. Sanchez-Cortes, *J. Phys. Chem. C*, 2013, **117**, 16203.
37 J. Kubackova, I. Izquierdo-Lorenzo, D. Jancura, P. Miskovsky and S. Sanchez-Cortes, *Phys. Chem. Chem. Phys.*, 2014, **16**, 11461.
38 J. Kubackova, G. Fabriciova, P. Miskovsky, D. Jancura and S. Sanchez-Cortes, *Anal. Chem.*, 2015, **87**, 663.
39 L. Guerrini, A. E. Aliaga, J. Carcamo, J. S. Gomez-Jeria, S. Sanchez-Cortes, M. M. Campos-Vallette and J. V. Garcia-Ramos, *Anal. Chim. Acta*, 2008, **624**, 286.
40 S. Mishra, V. Vallet, L. V. Poluyanov and W. Domcke, *J. Chem. Phys.*, 2006, **125**, 164327.
41 W. N. Leng and A. M. Kelley, *J. Am. Chem. Soc.*, 2006, **128**, 3492.
42 S. L. Kleinman, B. Sharma, M. G. Blaber, A. I. Henry, N. Valley, R. G. Freeman, M. J. Natan, G. C. Schatz and R. P. Van Duyne, *J. Am. Chem. Soc.*, 2013, **135**, 301.
43 J. P. Camden, J. A. Dieringer, J. Zhao and R. P. Van Duyne, *Acc. Chem. Res.*, 2008, **41**, 1653.
44 T. Butburee, Y. Bai, J. Pan, X. Zong, C. H. Sun, G. Liu and L. Z. Wang, *J. Mater. Chem. A*, 2014, **2**, 12776.
45 X. He, C. Yue, Y. S. Zang, J. Yin, S. B. Sun, J. Li and J. Y. Kang, *J. Mater. Chem. A*, 2013, **1**, 15010.
46 S. H. Jang, J. H. Yoon, Y. D. Huh and S. Yoon, *J. Mater. Chem. C*, 2014, **2**, 4051.
47 P. Li, X. N. Yan, F. Zhou, X. G. Tang, L. B. Yang and J. H. Liu, *J. Mater. Chem. C*, 2017, **5**, 3229.
48 G. Liu, W. Cai, L. Kong, G. Duan, Y. Li, J. Wang and Z. Cheng, *J. Hazard. Mater.*, 2013, **248**, 435.
49 Q. Zhao, G. Liu, H. Zhang, F. Zhou, Y. Li and W. Cai, *J. Hazard. Mater.*, 2017, **324**, 194.
50 G. Liu, W. Cai, L. Kong, G. Duan, Y. Li, J. Wang, G. Zuo and Z. Cheng, *J. Mater. Chem.*, 2012, **22**, 3177.